Materials & Design 243 (2024) 113039

Contents lists available at ScienceDirect

Materials & Design

journal homepage: www.elsevier.com/locate/matdes

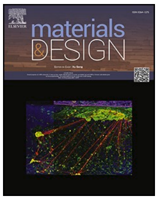

# Fabricating a single-crystal-like β grain structure of a near-β Ti alloy with unique variant selection by laser powder bed fusion

Tomonori Kitashima [a,b,*], Takanobu Hiroto [c], Dennis Edgard Jodi [a,d], Makoto Watanabe [a]

[a] *Research Center for Structural Materials, National Institute for Materials Science, 1-2-1 Sengen, Tsukuba, Ibaraki 305-0047, Japan*
[b] *Department of Materials, Kyushu University, 744 Motooka Nishi-ku, Fukuoka 819-0395 Japan*
[c] *Research Network and Facility Services Division, National Institute for Materials Science, 1-2-1 Sengen, Tsukuba, Ibaraki 305-0047, Japan*
[d] *Department of Materials Physics and Chemistry, Kyushu University, 744 Motooka Nishi-ku, Fukuoka 819-0395 Japan*

## ARTICLE INFO

*Keywords:*
Laser powder bed fusion
Titanium
Texture
Precipitation
Variant selection

## ABSTRACT

A near-β Ti alloy with a highly anisotropic single-crystal-like β grain structure was fabricated on a polycrystalline pure-Ti substrate by laser powder bed fusion (LPBF) using a flat-top laser with bidirectional scanning and 90° hatch rotation. The as-fabricated specimen had an acicular microstructure with 12 α variants. β-annealing followed by air-cooling revealed the growth of columnar β grains with a $\langle 001\rangle$ orientation in the build direction from the center outward with increasing height, which formed a highly anisotropic β grain structure with a $\langle 001\rangle$ orientation in the build direction and $\langle 100\rangle$ or $\langle 010\rangle$ orientation along the scan direction with low-angle grain boundaries (LAGBs) in the β matrix. The predominant $\langle 2\bar{1}\bar{1}0\rangle$-oriented and minor $\langle 10\bar{1}2\rangle$-oriented α phases precipitated in the $\langle 001\rangle$-oriented β matrix according to the Burgers orientation relationship. The $\langle 10\bar{1}2\rangle$-oriented α phase was found to form on some LAGBs. Notably, a single α variant was widely distributed without forming multiple-variant clusters across the highly anisotropic β grain structure.

## 1. Introduction

Additive manufacturing (AM) processes enable the fabrication of three-dimensional objects by the layering of materials, which enables the preparation of tailored microstructure and grain-structure distributions within parts. Traditionally, Ti-alloy parts used for high-temperature applications, such as high-pressure compressor blades in jet engines, undergo thermo-mechanical processing to achieve a microstructure comprising equiaxed α and lamellar structures—a bi-modal microstructure optimized for achieving creep and low-cycle-fatigue resistances [1]. While this bi-modal microstructure is distributed throughout the entire processed part, AM processes enable the formation of suitable microstructures in regions dominated by creep or fatigue.

Microstructural parameters affect fatigue properties of Ti alloys [2]. For example, large sizes of equiaxed α and prior β grains shorten their low-cycle-fatigue lifetime [3,4]. Notably, in α–β Ti alloys, the α-phase texture resulting from variant selection is crucial, as the formation of a single or a few of α variants degrades the fatigue properties [5,6]. Therefore, the formation of multiple α variants enhances fatigue resistance. The formation of grain structures, refinement of grains, and formation of several α variants using AM processes have been previously reported for Ti alloys ([7–10]). The details of α-variant selection during AM processes will be discussed later. A single-crystal structure offers superior creep resistance by mitigating detrimental grain-boundary effects, such as grain-boundary sliding and diffusion-induced grain-boundary migration. Single crystals of pure Ni and Ni-base superalloys have been successfully fabricated via powder bed fusion (PBF) without using single-crystal seeds [11–16]. However, there are limited reports on the formation of single-crystal structures in Ti alloys using AM processes. It is known that creep deformation in α-phase Ti alloys with a hexagonal-close-packed (*hcp*) lattice is highly anisotropic and dependent on the orientation of the creep load. Grains oriented along the *c*-axis of the *hcp* lattice parallel to the load direction exhibit greater resistance to creep compared to those oriented perpendicular to the load direction [17,18]. This phenomenon is mainly attributed to slower self-diffusion and solute diffusion along the *c*-axis as well as challenging activation of $(0001)\langle 11\bar{2}0\rangle$ basal and $\{10\bar{1}0\}\langle 11\bar{2}0\rangle$ prismatic slip systems in grains with the *c*-axis oriented parallel to the load direction [17,18]. The formation of single-crystal β grain structure and control of α-variant selection in Ti alloys, therefore, can facilitate the production of

---

[*] Corresponding author at: Research Center for Structural Materials, National Institute for Materials Science, 1-2-1 Sengen, Tsukuba, Ibaraki 305-0047, Japan.
*E-mail address:* KITASHIMA.Tomonori@nims.go.jp (T. Kitashima).

https://doi.org/10.1016/j.matdes.2024.113039
Received 14 February 2024; Received in revised form 28 April 2024; Accepted 21 May 2024

creep-resistant microstructures, offering enhanced flexibility in microstructure design for high-temperature applications, such as high-pressure compressor blades.

Single crystals have been fabricated by electron-beam PBF (EB-PBF) without the use of single-crystal seeds [11–15]. However, fabricating such single crystals via laser PBF is difficult owing to the use of Gaussian-type lasers, which form a semielliptical melt-pool geometry on the plane perpendicular to the scan direction (SD) because of their decaying intensity profile where the maximum intensity is at the spot center and zero intensity is along the beam radius [16]. Thus, the solidification-cell growth direction is continuously tilted from the edge to the center of the melt pool, which results in the formation of high-angle grain boundaries (HAGBs) and hinders continuous epitaxial growth in the build direction (BD) [16,19,20]. However, a flat-top laser with uniform intensity over the spot area [21] has been used to realize planar melt-pool geometry on the plane perpendicular to SD in pure Ni to enhance epitaxial growth aligned with the $\langle 001\rangle$ orientation of the face-centered cubic (fcc) lattice in the BD [16]. Moreover, the epitaxial growth in the $\langle 001\rangle$ direction was shown to deviate by 45° from the SD on the SD–hatch direction (HD) plane [22]. Consequently, using bidirectional laser scanning with 90° hatch rotation on the SD–HD plane yielded a single-crystal structure with $\langle 001\rangle$ and $\langle 101\rangle$ textures parallel to (‖) the BD and SD, respectively [16,22]. The preferential growth direction of cubic crystals, including fcc and body-centered cubic (bcc) crystals, is parallel to $\langle 001\rangle$ and is aligned along the highest-thermal-gradient direction at the solidification front during crystal growth [23–25]. Therefore, the planar melt pool produced during LPBF using a flat-top laser can also be used to form single crystals of other metals or alloys with a cubic crystal structure [16].

In Ti alloys, the bcc β phase solidifies from a molten state. With LPBF, the growth of columnar β grains occurs predominantly in the BD during solidification [10,26–30], which can result in a strong $\langle 001\rangle\|$BD texture and weaker textures in the in-plane direction on the SD–HD plane [29,30]. Furthermore, bidirectional scanning using a Gaussian-type laser on β-Ti alloys has led to strong $\langle 001\rangle\|$BD and $\langle 100\rangle\|$SD textures with 90° HD rotation between layers or strong $\langle 001\rangle\|$SD and $\langle 101\rangle\|$BD textures with no HD rotation between layers, which are accompanied by the formation of HAGBs [31,32]. For the growth of the single-crystal structure, it is important to minimize the deviation of $\langle 001\rangle$-oriented bcc growth from the BD at the rear of the melt pool on the SD–BD plane and at the relatively narrow center of the planar melt pool on the HD–BD plane. However, optimizing temperature distribution and melt-pool geometry for Ti alloys is essential because these factors are strongly dependent on material types, such as Ti or Ni, and their thermal properties [33,34]. For instance, in Ti–6Al–4 V, the high laser absorption by powder particles and low thermal conductivity leads to a longer tailing and higher depth-to-width ratio of the melt pool compared to materials such as Inconel 718, 304 stainless steel, and AlSi10Mg [33].

The use of a flat-top laser during LPBF enables the formation of a wider and flatter region on the melt-pool surface compared with the case of using a Gaussian-type laser, which enhances $\langle 001\rangle$-oriented epitaxial growth along the BD and promotes grain selection, suppressing HAGB formation.

A single β grain can transform into 12 variants of the α phase [35] according to the Burgers orientation relationship (BOR) [36] during cooling in the (α + β) dual-phase region. However, certain α variants form preferentially (i.e., variant selection) because of underlying factors such as strain energy accommodation [35,37,38], dislocations [39], β grain misorientation [37,40–46], the prior β-grain-boundary plane [47], and the texture memory effect [48,49]. α-variant selection plays an influential role in the evolution of textures, and the texture of the α phase affects the mechanical properties including creep resistance as mentioned before [50,51]. This study explored the feasibility of using a flat-top laser in LPBF to form highly anisotropic single-crystal-like β grain structures without HAGBs to tailor the anisotropic textures and α variant selection of near-β Ti alloys. Ti–6Al–2Sn–4Zr–6Mo (wt%) (Ti-6246) was selected as a representative near-β Ti alloy.

## 2. Materials and methods

Specimens were fabricated in an Ar atmosphere using a selective laser melting system (SLM 280 HL; SLM Solutions, Germany) equipped with a flat-top laser having a beam diameter of 700 μm. The beam profile of the flat-top laser in the SLM 280-type machine was detailed by Pilz et al. [29]. To observe the melt-pool geometry, single tracks of the laser were analyzed by using Ti-6246 plates (TIMET, USA) without a powder coating. The laser power and scan speed in the single-track analysis were varied in the range of 250–350 W and 100–450 mm/s, respectively. Plasma-atomized Ti-6246 powder (Advanced Powders & Coatings, Inc., Canada) was used to fabricate multilayers. The $D_{10}$, $D_{50}$, and $D_{90}$ values of the powder size distribution were 25.3, 41.1, and 63.7 μm, respectively. The β-transus temperature of Ti-6246 was approximately 1221 K. Multilayers were fabricated by using the following combination of optimized laser parameters: a laser power of 300 W, scan speed of 250 mm/s, hatch space of 120 μm, and layer thickness of 30 μm. Laser scanning was performed bidirectionally with 90° rotation of the HD at each layer. In this study, the BD was represented by the Z axis, and the SD was parallel to the X and Y axes and perpendicular to the Z axis. The HD and SD changed at each layer because of the 90° rotation of the HD. Cylindrical specimens with a diameter of 12 mm and height of 30 mm were fabricated on polycrystalline pure-Ti substrates. The powder stage was not heated. After fabrication, the specimens were first heated in an Ar-filled quartz capsule at 1233 K in the β region for 1.2 ks and then air-cooled. All specimens were sectioned and ground with abrasive paper (#320 and #600) and were mechanically polished by using diamond (9, 3, and 1 μm) and colloidal silica suspensions. Scanning electron microscopy (SEM; JEOL JSM-7001F) and electron backscatter diffraction (EBSD) were performed to characterize the microstructures of the specimens. EBSD analysis was conducted on SD/HD–BD cross-sections with dimensions of 800 μm × 6400 μm, 800 μm × 1200 μm, 37 μm × 80 μm, and 16 μm × 35 μm at step sizes of 4, 2, 0.1, and 0.06 μm. EBSD data with confidence index values of >0.1 were analyzed using TSL OIM 8. The subgrain boundaries, low-angle grain boundaries (LAGBs), and HAGBs were classified according to misorientations of 2°–5°, 5°–15°, and >15°, respectively. In the pole figure analysis, grains were defined by adopting a grain tolerance angle of 2° to distinguish α variants formed in β-phase regions with misorientations of >2°. The constituent phases were identified by X-ray diffraction (XRD) using a SmartLab diffractometer (Rigaku, Japan) with Cu Kα ($\lambda = 1.5418$ A) radiation generated at 45 kV and 200 mA.

## 3. Results and discussion

### 3.1. As-fabricated and β-annealed microstructures

As shown in Fig. 1, an acicular microstructure was observed at a height of 29 mm in the as-fabricated specimens (Fig. 1a). In Ti alloys, the β phase transforms to martensitic phases such as $\alpha'$ or $\alpha''$ during rapid cooling [52–54]. In Ti-6246, $\alpha''$ phase formation has previously been detected in microstructures after quenching from high temperatures (e.g., 1143 K–1253 K) in the (α + β) dual-phase region and β single-phase region (for example, see [55,56]).

Fig. 2 shows that the XRD pattern of the as-fabricated specimen indicated a microstructure with α and β phases, which was attributed to the decomposition of the martensitic $\alpha''$ phase after its formation from the β phase to α and β phases. The decomposition of the $\alpha''$ phase can be promoted by heat accumulation and a low cooling rate if the laser-scanning speed during fabrication is lowered [57–59]. In this study, grain boundaries were occasionally detected by observing thin lines of the grain-boundary α in SEM images (arrow A in Fig. 1a). The adjacent β grains across such grain boundaries exhibited minor misorientations. For example, inverse pole figure (IPF) maps of the α phase in the BD

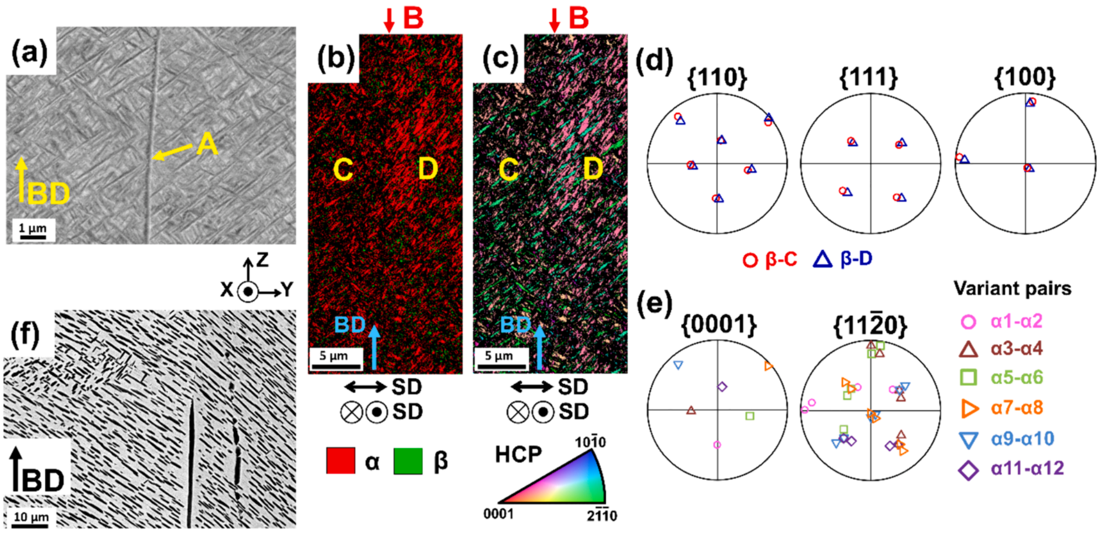

**Fig. 1.** (a) Backscattered-electron image of the as-fabricated microstructure including the grain boundary α (arrow A) on the cross-section parallel to the build direction (BD). (b) Electron backscatter diffraction (EBSD) phase map and (c) inverse pole figure (IPF) map of the α phase in the BD. (d) Pole figures of the β phase in grains C and D. (e) Pole figures of the α phase in grain D. (f) Backscattered-electron image of the β-annealed microstructure on the cross-section parallel to the BD. The analysis area in (c) has dimensions of 16 μm × 35 μm with a step size of 0.06 μm.

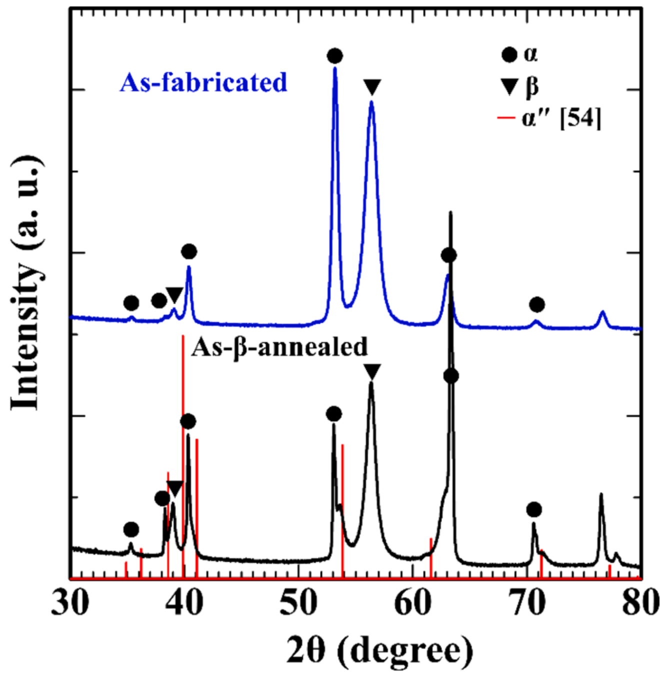

**Fig. 2.** X-ray diffraction patterns of the as-fabricated and β-annealed specimens. Peaks corresponding to α″, as observed in a Ti–Mo system [54], are superimposed on the peaks corresponding to the β-annealed specimen.

showed two β grains C and D across the grain boundary B (Fig. 1c). Grains C and D had a misorientation of only 5° (Fig. 1d), which indicates almost parallel bcc alignment between them. The precipitated α phase was ultrafine, and twelve α variants with six {0001}-pole pairs were detected in grain D (Fig. 1e). The as-fabricated specimen was heated at 1233 K in the β single-phase region for 1.2 ks and then air-cooled. Subsequently, thicker α precipitates and grain-boundary α were clearly observed (Fig. 1f). The XRD results indicated that the β-annealed microstructure comprised α and β phases formed during the air-cooling afterward (Fig. 2). The feet of the α peaks were slightly broadened between the α and α″ peak positions.

### *3.2. Crystallographic texture and β grain misorientation of the β-annealed specimen*

Fig. 3 shows IPF maps in the BD for the (Fig. 3a–d) β and (Fig. 3e) α phases and (Fig. 3f–i) in the X direction along the SD/HD for the β phase on the Y–Z (SD/HD–BD) plane of the β-annealed specimen at heights of 15, 20, 25, and 30 mm.

The centerline of the cylindrical specimen is marked by a dashed line. IPF maps along the Y direction (SD/HD) are given in the Supplementary Material (Fig. S1). The formation of thicker α precipitates during air-cooling revealed the orientation distribution of the β grains (Fig. 3a–d). Narrow columnar β grains with various orientations close to $\langle 001\rangle$, $\langle 101\rangle$, and $\langle 111\rangle$ grew at the height of 15 mm (Fig. 3d). β grains with the $\langle 001\rangle$||BD orientation grew and became thicker with increasing height, whereas grains with other orientations grew obliquely upward and outward especially at the heights of 20, 25, and 30 mm (Fig. 3a–c). Concurrently, a uniform $\langle 001\rangle$||BD texture became dominant from the center outward at the heights of 25 and 30 mm and uniform $\langle 100\rangle$||SD/HD and $\langle 010\rangle$||SD/HD textures gradually formed with increasing height (Fig. 3f–g, Fig. S1a and b in the Supplementary Material). However, the $\langle 100\rangle$ and $\langle 010\rangle$ orientations tended to align to the SD/HD after the $\langle 001\rangle$ orientation aligned to the BD. For example, at a height of 20 mm, the $\langle 100\rangle$ orientation of β grains with the $\langle 001\rangle$||BD texture inclined from SD/HD (boxes in Fig. 3c and h). At a height of 25 mm, most grains at the same distance from the center showed the $\langle 100\rangle$ orientation along the SD/HD (red-dashed box in Fig. 3g). Similarly, $\langle 001\rangle$||BD and $\langle 101\rangle$||SD/HD textures at a height of 25 mm (blue-dashed box in Fig. 3b and g) transformed into $\langle 001\rangle$||BD and $\langle 100\rangle$||SD/HD textures at a height of 30 mm with the same distance from the center (blue-dashed box in Fig. 3a and f).

As shown in Fig. 4, the growth of β grains at the center with $\langle 001\rangle$||BD, $\langle 100\rangle$||SD/HD, and $\langle 010\rangle$||SD/HD textures was indicated by an increase in the maximum intensity of the IPF maps in the X, Y and Z directions (IPF-X, IPF-Y, IPF-Z) for a region spanning 800 μm × 1200 μm and at heights of 30 (Fig. 4a–c) and 15 mm (Fig. 4e–g). Contour maps of IPF-Z, IPF-X, and IPF-Y for the β phase were obtained for an area of 800 μm × 1200 μm at heights of 15, 20, 25, and 30 mm at the center and both sides of the central area (Fig. 4i–k). The intensity increased with height for the $\langle 001\rangle$, $\langle 100\rangle$, and $\langle 010\rangle$ orientations. Moreover, the maximum intensities of IPF-X and IPF-Y for the β phase increased later than that of IPF-Z because the $\langle 100\rangle$ and $\langle 010\rangle$ orientations aligned with the SD/HD

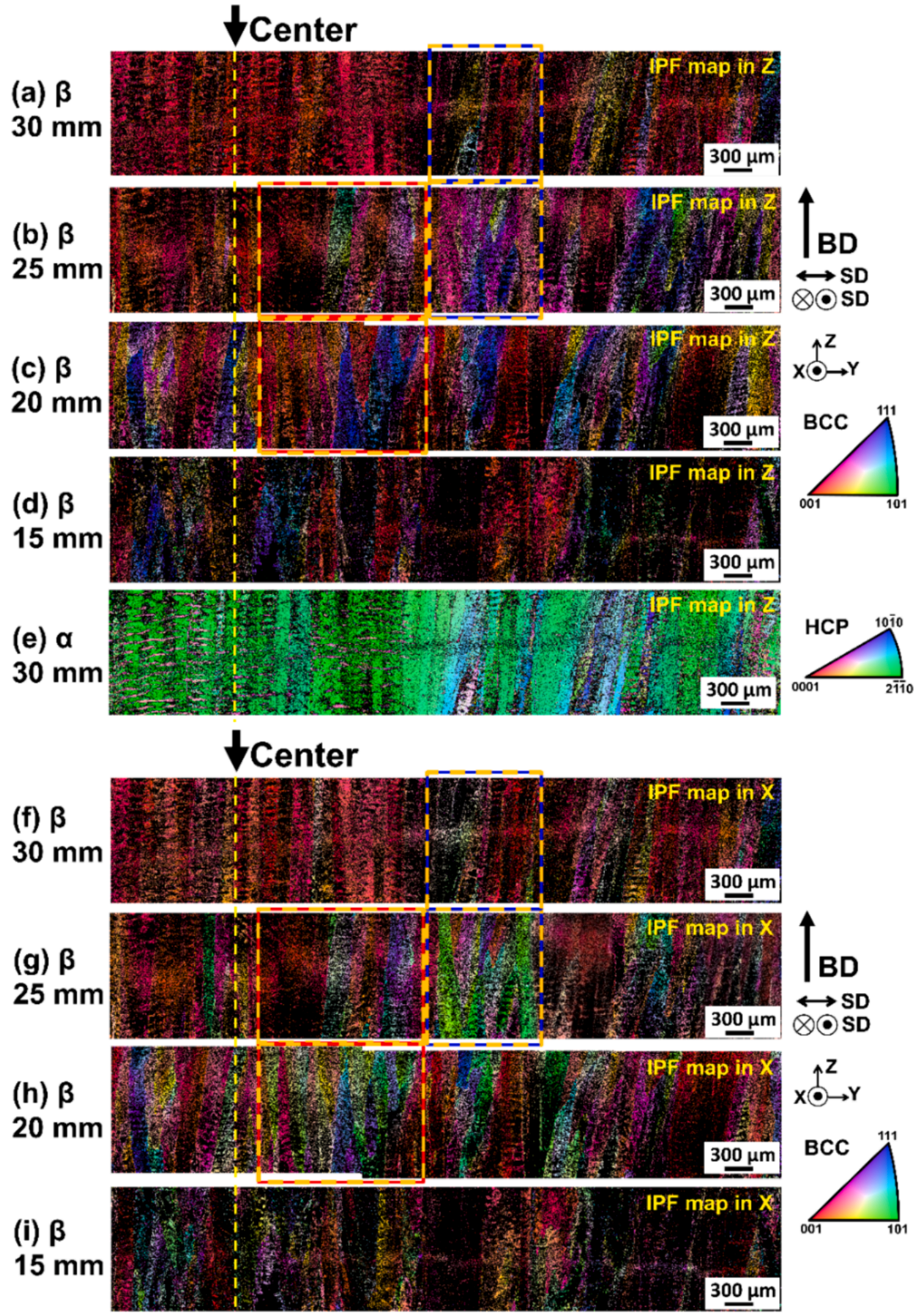

**Fig. 3.** IPF maps of (a–d) β and (e) α phases in the *Z* direction (BD) at heights of (a, e) 30, (b) 25, (c) 20, and (d) 15 mm for the as-β-annealed specimen. IPF maps of the β phase in the *X* direction (SD/HD) at heights of (f) 30, (g) 25, (h) 20, and (i) 15 mm for the as-β-annealed specimen. The analyzed area has dimensions of 800 μm × 6400 μm with a step size of 4 μm. The centerline of the cylindrical specimen is shown by a dashed line.

later than the $\langle 0\,0\,1\rangle$ orientation aligned with the BD.

The α phase in the $\langle 0\,0\,1\rangle$-oriented β region uniquely exhibited a predominant $\langle 2\bar{1}\bar{1}0\rangle$ orientation in the BD (Fig. 3e), which is because $[11\bar{2}0]$ exhibits a 5° misorientation from $[0\,0\,1]$ when $[1\bar{2}10]$ is aligned to $[1\,1\,1]$ during formation of the α phase according to the BOR [60]. The $\langle 2\bar{1}\bar{1}0\rangle$ intensity was greater at a height of 30 mm than at 15 mm (Fig. 4d, h) because β grains with the $\langle 0\,0\,1\rangle \| \mathrm{BD}$ texture grew at 30 mm. The misorientation of adjacent β grains was within the range for LAGBs. Fig. 5 shows the IPF maps along the *Z*, *X*, and *Y* directions for the β (Fig. 5a–c) and α phases (Fig. 5d–f) at the center of a β-annealed specimen at a height of 30 mm. The $\{0\,0\,1\}/\{1\,1\,0\}$-pole figures of the β phase with $\langle 0\,0\,1\rangle \| \mathrm{BD}$, $\langle 1\,0\,0\rangle \| \mathrm{SD/HD}$, and $\langle 0\,1\,0\rangle \| \mathrm{SD/HD}$ textures in the analyzed area presented a cubic-type $\{1\,0\,0\}$ $\langle 0\,0\,1\rangle$ texture component (Fig. 5g). The point-to-point misorientation of the β phase along the arrow in Fig. 5a was less than 8° (Fig. 5h). Notably, the formation of the grain-boundary α was observed along LAGBs (arrows in Fig. 5d).

Fig. 6 shows IPF maps of the β (Fig. 6a) and α phases (Fig. 6b) in the BD for the magnified area near the grain boundaries in Fig. 5a and d. Grain boundary α formed continuously on grain boundaries between grains A and B and occasionally between grains A and C. The point-to-point misorientation along the arrow in Fig. 6a indicates formation of grain-boundary α along LAGBs (Fig. 6d). The β grain misorientation can be further minimized by increasing the height of the specimen or further optimizing the process parameters. These results demonstrated that a flat-top laser can be used in LPBF to fabricate Ti-6246 with a bcc single-crystal structure and LAGBs without using single-crystal seeds.

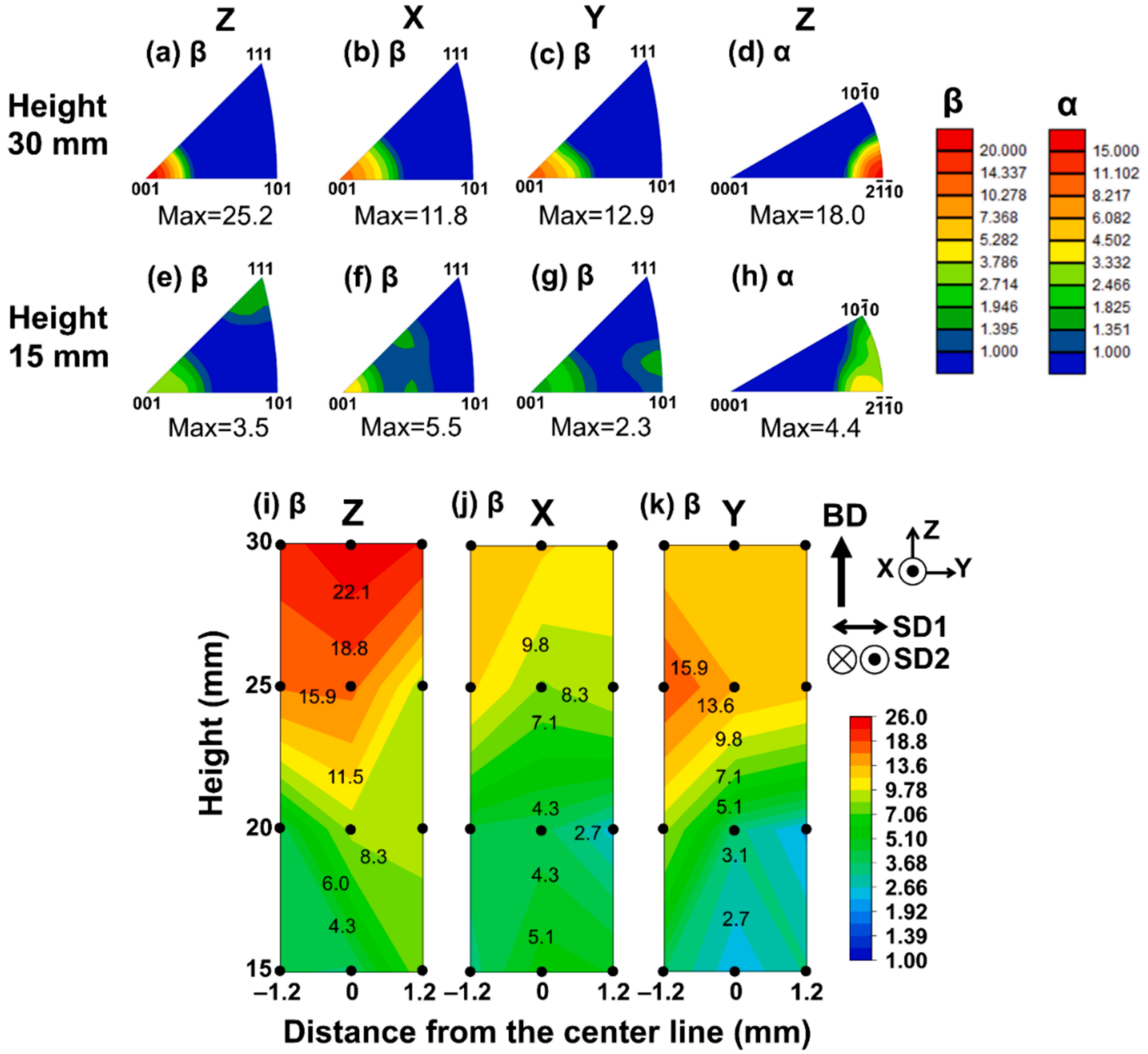

**Fig. 4.** IPF maps of the (a–c, e–g) β and (d, h) α phases in the *Z* (BD), *X*, and *Y* (SD/HD) directions at heights of 30 and 15 mm in a β-annealed specimen. Contours of maximum intensity for (i) IPF-Z, (j) IPF-X, and (k) IPF-Y of the β phase of a β-annealed specimen obtained for an 800 μm × 1200 μm area on the Y–Z (SD/HD–BD) plane at the center and on both sides of the central area at a height of 15–30 mm.

### 3.3. *Texture formation of a single-crystal-like β grain structure*

The development of textures in LPBF using Gaussian-type and flat-top lasers has been extensively studied for cubic metallic alloys including Ti alloys [10,19,27–32,61,62]. With a Gaussian-type laser, increasing the energy density, such as by reducing the scan speed and increasing the laser power, yields a deeper melt pool. The deep melt pool causes ⟨0 0 1⟩ epitaxial growth from a semielliptical fusion line toward the melt-pool center upward on the HD–BD plane, which is accompanied by competitive grain growth [19,61]. In addition, the continuously inclined ⟨0 0 1⟩ epitaxial growth relative to the BD on the SD–BD plane and relative to the SD on the SD–HD plane at the rear of the melt pool cause the formation of ⟨1 0 1⟩||BD and/or ⟨1 1 1⟩||BD textures owing to the curved surface of the melt pool [19,61]. Decreasing the energy density, such as by increasing the scan speed and decreasing the laser power, generates a shallower melt pool with a less curved surface, which promotes solidification-cell growth in the BD [19,61]. Thus, the laser scan speed is a highly influential process parameter on the melt-pool geometry. Increasing the scan speed is effective for decreasing the depth-to-width ratio and decreasing the depth of the melt pool [63,64], although it tends to lead to a finer grain size because of the faster cooling rate [65]. A flat-top laser can be used to obtain a shallow and planar melt pool at low laser scan speeds [16,66]. Fig. 7 shows the backscattered-electron images of the cross-section of fusion tracks scanned by the flat-top laser in this study. A faster scan speed resulted in a narrower, shallower, and flatter melt-pool geometry. Notably, under an insufficient laser energy density, intensity deviations in the flat-top beam profile [29] may lead to an inhomogeneous temperature distribution on the plate surface. This can induce inhomogeneous thermal Marangoni flows dominantly in a narrow and shallow melt pool, leading to the formation of an asymmetric melt pool, as shown in Fig. 7(c). Even when a flat-top laser beam scans over the powder bed at a low energy density, irregular flows can arise owing to the dominance of spherical melt flow and their merging, accompanied by thermal Marangoni flow [67,68]. Consequently, this can also generate an asymmetric melt pool. In this study, a laser power of 300 W and scan speed of 250 mm/s yielded a planar and symmetric fusion line at the center. These settings were adopted to fabricate multilayer specimens, which enhanced the growth of a bcc structure along the ⟨0 0 1⟩ orientation close to the BD. The bcc β phase grows fastest along the ⟨0 0 1⟩ orientation, which is aligned with the highest-thermal-gradient direction at the solidification front (i.e., almost perpendicular to the melt-pool surface) [23–25]. Therefore,

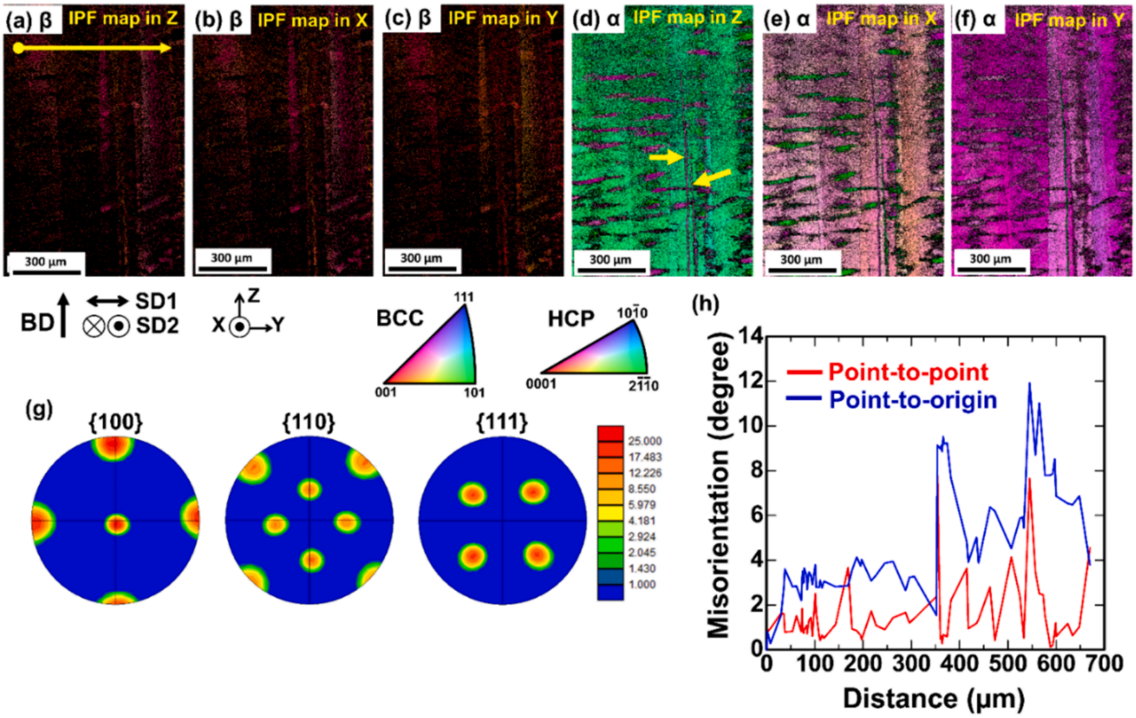

**Fig. 5.** IPF maps of the (a–c) β and (d–f) α phases in the *Z* (BD), *X*, and *Y* (SD/HD) directions on the *Y*–*Z* (SD/HD–BD) plane at a height of 30 mm. The analysis area has dimensions of 800 µm × 1200 µm with a step size of 2 µm. (g) Pole figures of the β phase obtained from the same area as (a). (h) Misorientation profiles along the arrow in (a).

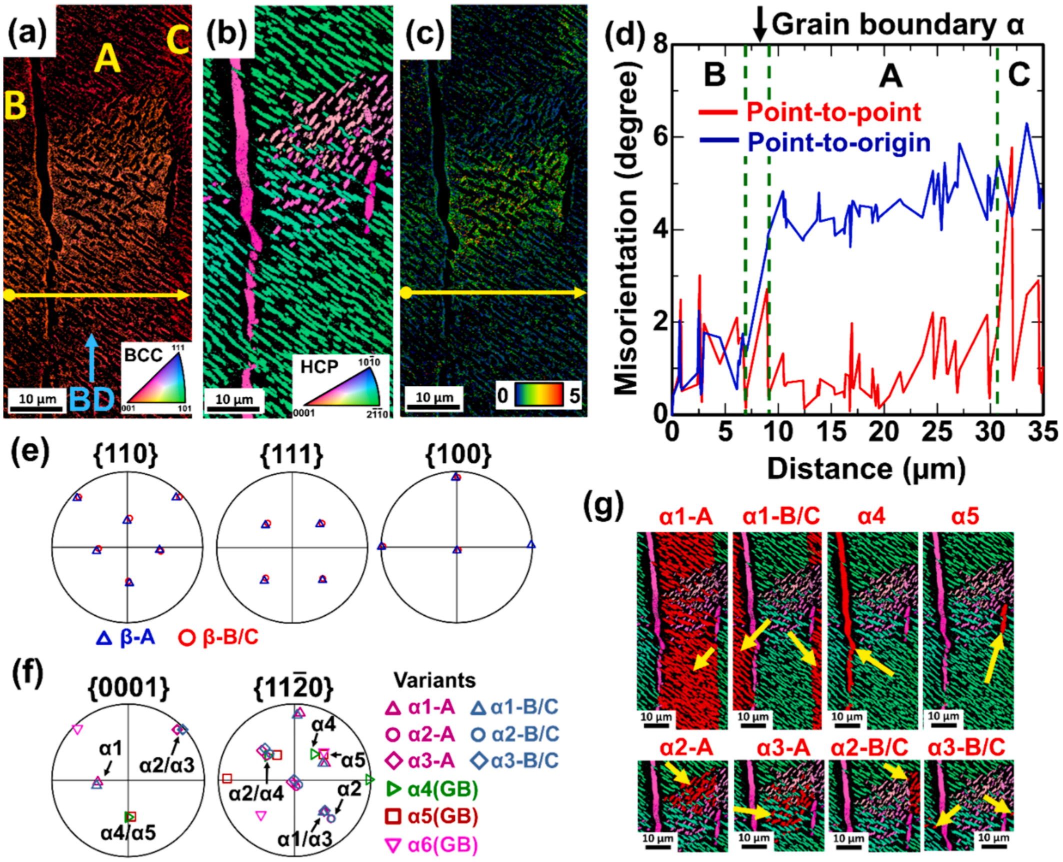

**Fig. 6.** IPF maps of the (a) β and (b) α phases in the *Z* direction (BD). (c) Kernel-averaged misorientation map at a height of 30 mm. The analysis area has dimensions of 37 µm × 80 µm with a step size of 0.1 µm. (d) Misorientation profiles along the arrows in (a) and (c). (e) Pole figures of the β phase of grains A, B, and C. (f) Pole figures of the α phase formed in grains A, B, and C and at grain boundaries. (g) Five α variants observed in the analysis area.

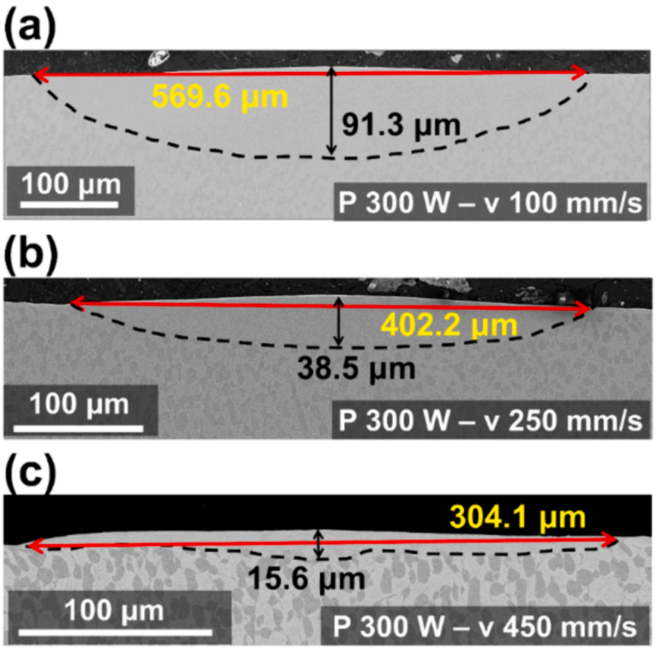

**Fig. 7.** Backscattered-electron images of the cross-sections of single fusion tracks scanned using a flat-top laser beam at different laser scan speeds: (a) 300 W and 100 mm/s, (b) 300 W and 250 mm/s, and (c) 300 W and 450 mm/s.

grains with the ⟨001⟩||BD texture grew epitaxially from the planar melt-pool surface outgrew grains with other textures in this study (Fig. 3a–d).

As noted previously, the alignment of the ⟨001⟩ orientation in the BD occurred earlier than the alignment of the ⟨100⟩ and ⟨010⟩ orientations to the SD/HD. In such a planar melt pool, the grain growth was more dominant in the BD than in the in-plane direction (i.e., perpendicular to the BD). One important difference between the single-crystal-like β grain structure of Ti-6246 in this study and the previously reported single-crystal structure of pure Ni [16,22] is the texture along the SD. Pure Ni had ⟨001⟩||BD and ⟨101⟩||SD textures, whereas Ti-6246 had ⟨001⟩||BD, ⟨100⟩||SD, and ⟨010⟩||SD textures. In pure Ni, the epitaxial growth of the fcc structure in the ⟨001⟩ orientation deviated by 45° from the SD at the rear of the melt-pool surface on the SD–HD plane [22]. Then, the 90° rotation of the bidirectional laser scanning for each layer resulted in the ⟨101⟩||SD texture [22]. In a study employing EB-PBF for a β Ti alloy, a shallow and wide melt pool was generated that resulted in the occasional growth with ⟨100⟩ or ⟨010⟩ orientations in the HD in addition to the growth with the ⟨001⟩ orientation in the BD at the sides despite the melt-pool surface being inclined by approximately 45° from the HD on the HD–BD plane [69]. Another study that used a laser to melt the surface of a Ni-base single-crystal superalloy substrate demonstrated that orthogonal dendrites grew along the [001], [100], and [010] directions from the curved melt-pool surface during scanning along the [100] direction on the (001) plane [70,71]. In addition, [010] dendritic growth, which was perpendicular to the SD and parallel to the substrate surface, was observed at the sides of the melt pool near the surface [70,71]. In this study, however, the epitaxial growth of the bcc structure with the ⟨010⟩ orientation (i.e., perpendicular to the SD and parallel to the HD) can be more dominant than that parallel to the SD on the SD–HD plane as the laser moved in the SD. In contrast to the case of pure Ni [16,22], a higher laser-scanning speed in this study caused the formation of a more elongated melt-pool tail in the SD. This promoted epitaxial growth with a ⟨010⟩ orientation in the HD (i.e., perpendicular to the SD) at the sides of the melt pool. These facts explain why the ⟨001⟩ orientation of the β grains aligned to the BD before the ⟨100⟩ and ⟨010⟩ orientations aligned to the HD and led to the development of the ⟨100⟩||SD/HD and ⟨010⟩||SD/HD textures during the bidirectional laser scanning with 90° HD rotation between layers (Fig. 3f and g, Fig. S1a and b in the Supplementary Materials). Thus, the dominant epitaxial growth of the ⟨001⟩ orientation in the BD and ⟨010⟩ orientation in the HD led to the single-crystal-like β grain structure with ⟨001⟩||BD, ⟨100⟩||SD/HD, and ⟨010⟩||SD/HD textures.

### 3.4. Distribution of α variants in the β-annealed specimen

The growth of ⟨001⟩-oriented β grains in the BD with LAGBs was observed in the β-annealed specimens. The orientations of β grains B and C (Fig. 6a) matched in terms of the bcc poles of {110}, {111}, and {100} (Fig. 6e). In contrast, β grains A and B/C exhibited a 5° misorientation in the pole figures (Fig. 6e). In these β grains, the precipitated α phase exhibited predominant $\langle 2\bar{1}\bar{1}0\rangle \| \mathrm{BD}$ and minor $\langle 10\bar{1}2\rangle \| \mathrm{BD}$ textures (Fig. 6b). Grain-boundary α with the $\langle 10\bar{1}2\rangle \| \mathrm{BD}$ texture formed on the LAGBs. Pole figure analysis (Fig. 6e and f) indicated that the α phases formed under the BOR (i.e., $\{0001\}_\alpha \| \{110\}_\beta$ and $\langle 2\bar{1}\bar{1}0\rangle_\alpha \| \langle 111\rangle_\beta$). Thus, the α phases comprised six variants with four {0001} poles. Furthermore, the α precipitate with the $\langle 10\bar{1}2\rangle \| \mathrm{BD}$ texture had two variants α2 and α3 (Fig. 6g). Inter-variant misorientation can be classified into six types of axis–angle pairs [72]. Variants α2/α3 of the α precipitates and α4/α5 of grain-boundary α shared common {0001} axes and rotated 10° about the common axes (Fig. 6f), which suggests that the axis–angle misorientations of α2/α3 and α4/α5 were of the [0001]/10.53° type [72]. In addition, α1/α3 and α2/α4 shared $[11\bar{2}0]$ axes rotated 120° about the common axes, which suggests that they belonged to the $[11\bar{2}0]$/60° type [72]. The formation of multiple variants of α laths with a basket-weave microstructure and misorientations of $[11\bar{2}0]$/60° and [0001]/10.53° types have been reported for forged [37,40,41] and additively manufactured α–β Ti alloys [26,73,74].

Several previous studies have considered α variant selection of α–β and near-β Ti alloys in AM [26,30,73,74]. In this study, a unique α variant was identified in Ti-6246 after β annealing at 1233 K for 20 min followed by air-cooling. α variant selection is greatly affected by the evolution of the microstructure during the transformation of the β phase to α + β phases. During slow cooling from the single β phase region, grain-boundary α first forms at β-grain boundaries, having the BOR with one of the adjacent β grains. Then, Widmanstätten colonies grow from the grain-boundary α into the β grain with the same orientation as the grain-boundary α according to the BOR [40,41,43,75]. In this case, the first colonies to form dominate and disrupt other colonies occupying the β grain, which causes the formation of only a few α colonies or a single α colony in each grain depending on the cooling rate. Therefore, a stronger β-phase microtexture leads to the stronger formation of the α-phase microtexture. In contrast, more rapid cooling leads to the development of basket-weave or acicular microstructures that form multiple-variant clusters of α laths with inter-variant misorientations in the β matrix [37,38]. The clustering of multiple variants has mainly been attributed to minimization of the transformation-induced strain [26,35,37,38,73,74]. For example, in the as-cast β-rich Ti alloy, fine α phase precipitated and clusters of three α variants with an inter-variant misorientation of $[11\bar{2}0]$/60° were dominantly formed during the growth of semi-coherent α phase with residual elastic energy [38]. In the present study, however, β-annealing followed by air-cooling predominantly led to $\langle 2\bar{1}\bar{1}0\rangle$-oriented α precipitation with a widely distributed α1 variant across LAGBs in highly anisotropic single-crystal-like β grains, and clusters of multiple variants did not form. Such a large selection of a single α variant across LAGBs has not been previously reported. The strain accumulation induced by fabrication can be reduced by β-annealing, although a strain gradient region persisted in the β grain (e.g., the region shown in the kernel-average misorientation map with variants α2/α3 in Fig. 6c). The application of LPBF using a flat-top laser to pure Ni [76] primarily caused the low dislocation density during annealing between 873 and 1273 K for 16 h and the arrangement of statistically stored dislocations instead of geometrically necessary dislocations, which resulted in an insignificant change in the cell-wall misorientation. The low dislocation density observed in the specimen derived from the flat-top laser further decreased with increasing annealing temperature and annealing duration, causing static recovery [76]. Herein, the dislocation density in the β matrix of the as-fabricated specimen may have been inherently low because of fabrication using a flat-top laser beam. In addition, the as-fabricated specimen was heat-treated at 1233 K in the β-single-phase region for 20 min, which is 12 K above the β-transus temperature. This β annealing likely altered the dislocation density and morphology within the β matrix. The process of α-variant selection in this study may be associated with dislocation density, morphology, and types, such as edge or screw dislocations, present in the β matrix [39], which can be affected by annealing temperature, annealing duration, and cooling rate. The effect of such dislocation or cell distributions on the single-variant distribution observed in this study will be analyzed in future studies.

## 4. Conclusions

The single-crystal structure exhibits superior creep resistance, while creep deformation of the α-phase along the *c*-axis of the *hcp* lattice is much harder than deformation perpendicular to the *c*-axis. The application of LPBF using a flat-top laser to Ti-6426 resulted in the formation of a highly anisotropic single-crystal-like β grain structure with $\langle 001\rangle \| \mathrm{BD}$, $\langle 100\rangle \| \mathrm{SD/HD}$, and $\langle 010\rangle \| \mathrm{SD/HD}$ textures and LAGBs without requiring the use of single-crystal seeds. β-annealing followed by air-cooling induced precipitation of a predominant $\langle 2\bar{1}\bar{1}0\rangle$-oriented α phase and minor $\langle 10\bar{1}2\rangle$-oriented α phase from the $\langle 001\rangle$-oriented β matrix under the BOR. A $\langle 10\bar{1}2\rangle$-oriented grain-boundary α was also observed along some LAGBs. Notably, a single α variant was widely distributed in the β single-crystal-like structure without forming multiple-variant clusters.

The *c*-axis of the single α variant was almost perpendicular to the BD and deviated by ∼45° from the SD according to the BOR. This indicates that aligning the ⟨0001⟩ orientation of the single α variant in the single-crystal β-grain structure along the highest-load direction of the Ti-alloy object can improve creep resistance. Furthermore, if we can align the *c*-axis perpendicular to the BD and to the SD through variant selection, it would expand the scope for microstructure design flexibility, which can be focused in future research. The results of this study provide novel insights into the process of obtaining single-crystal bcc structures in β-Ti alloys and controlling α variant selection in near-β Ti alloys for high-temperature applications of LPBF products such as high-pressure compressors used in jet engines.

## CRediT authorship contribution statement

**Tomonori Kitashima:** Writing – original draft, Resources, Project administration, Investigation, Funding acquisition, Formal analysis, Data curation, Conceptualization. **Takanobu Hiroto:** Writing – review & editing, Resources, Investigation, Formal analysis, Data curation. **Dennis Edgard Jodi:** Writing – review & editing, Investigation, Data curation, Conceptualization. **Makoto Watanabe:** Writing – review & editing, Resources, Project administration, Funding acquisition.

## Declaration of competing interest

The authors declare that they have no known competing financial interests or personal relationships that could have appeared to influence the work reported in this paper.

## Data availability

The data that has been used is confidential.

## Acknowledgments

The authors thank Dr. Miwako Takano, Mr. Masaru Suzuki, Ms. Chiho Togashi, Mr. Koji Nakazato, and Mr. Masahiko Kawasaki of the National Institute for Materials Science for their assistance.

### *Funding*

This research was supported in part by Amada Foundation, Japan (AF-2022215-B3).

## Appendix A. Supplementary data

Supplementary data to this article can be found online at https://doi.org/10.1016/j.matdes.2024.113039.

## References

[1] G. Lütjering, Influence of processing on microstructure and mechanical properties of (α+β) titanium alloys, Mater. Sci. Eng. A 243 (1998) 32–45, https://doi.org/10.1016/S0921-5093(97)00778-8.
[2] L. Wanger, J.K. Bigoney, Fatigue of titanium alloys, in: C. Leyens, M. Peters (Eds.), Titanium and Titanium Alloys: Fundamentals and Applications, Wiley VHC Verlag, Weinheim, 2003, pp. 153–185.
[3] M. Sen, S. Suman, S. Mukherjee, T. Banerjee, S. Sivaprasad, S. Tarafder, A. Bhattacharjee, S.K. Kar, Low cycle fatigue behavior and deformation mechanism of different microstructures in Ti-5Al-5Mo-5V-3Cr alloy, Int. J. Fatigue 148 (2021) 106238, https://doi.org/10.1016/j.ijfatigue.2021.106238.
[4] Y. Mahajan, H. Margolin, Low cycle fatigue behavior of Ti-6AI-2Sn-4Zr-6Mo: Part I. The role of microstructure in low cycle crack nucleation and early crack growth, Metall. Trans. A 13 (1982) 257–268, https://doi.org/10.1007/BF02643316.
[5] R. Shi, Y. Wang, Variant selection during α precipitation in Ti–6Al–4V under the influence of local stress – A simulation study, Acta Mater. 61 (2013) 6006–6024, https://doi.org/10.1016/j.actamat.2013.06.042.
[6] R. Whittaker, K. Fox, A. Walker, Texture variations in titanium alloys for aeroengine applications, Mater. Sci. Technol. 26 (2010) 676–684, https://doi.org/10.1179/026708310X12635619988186.
[7] M.S.K.K.Y. Nartu, B.A. Welk, S.A. Mantri, N.L. Taylor, G.B. Viswanathan, N. B. Dahotre, R. Banerjee, H.L. Fraser, Underlying factors determining grain morphologies in high-strength titanium alloys processed by additive manufacturing, Nat. Commun. 14 (2023) 3288, https://doi.org/10.1038/s41467-023-38885-9.
[8] M. Neikter, P. Åkerfeldt, R. Pederson, M.L. Antti, V. Sandell, Microstructural characterization and comparison of Ti-6Al-4V manufactured with different additive manufacturing processes, Mater. Charact. 143 (2018) 68–75, https://doi.org/10.1016/j.matchar.2018.02.003.
[9] S.A. Mantri, R. Banerjee, Microstructure and micro-texture evolution of additively manufactured β-Ti alloys, Addit. Manuf. 23 (2018) 86–98, https://doi.org/10.1016/j.addma.2018.07.013.
[10] M. Simonelli, Y.Y. Tse, C. Tuck, On the texture formation of selective laser melted Ti–6Al–4V, Metall. Mater. Trans. A 45 (2014) 2863–2872, https://doi.org/10.1007/s11661-014-2218-0.
[11] E. Chauvet, C. Tassin, J.J. Blandin, R. Dendievel, G. Martin, Producing Ni-base superalloys single crystal by selective electron beam melting, Scripta Mater. 152 (2018) 15–19, https://doi.org/10.1016/j.scriptamat.2018.03.041.
[12] P. Fernandez-Zelaia, M.M. Kirka, A.M. Rossy, Y. Lee, S.N. Dryepondt, Nickel-based superalloy single crystals fabricated via electron beam melting, Acta Mater. 216 (2021) 117133, https://doi.org/10.1016/j.actamat.2021.117133.
[13] M.R. Gotterbarm, A.M. Rausch, C. Körner, Fabrication of single crystals through a μ-Helix grain selection process during electron beam metal additive manufacturing, Metals 10 (2020) 313, https://doi.org/10.3390/met10030313.
[14] C. Körner, M. Ramsperger, C. Meid, D. Bürger, P. Wollgramm, M. Bartsch, G. Eggeler, Microstructure and mechanical properties of CMSX-4 single crystals prepared by additive manufacturing, Metall. Mater. Trans. A 49 (2018) 3781–3792, https://doi.org/10.1007/s11661-018-4762-5.
[15] J. Pistor, C. Körner, A novel mechanism to generate metallic single crystals, Sci. Rep. 11 (2021) 24482, https://doi.org/10.1038/s41598-021-04235-2.
[16] D.E. Jodi, T. Kitashima, Y. Koizumi, T. Nakano, M. Watanabe, Manufacturing single crystals of pure nickel via selective laser melting with a flat-top laser beam, Addit. Manuf. Lett. 3 (2022) 100066, https://doi.org/10.1016/j.addlet.2022.100066.
[17] W. Li, Z. Chen, J. Liu, Q. Wang, G. Sui, Effect of texture on anisotropy at 600 °C in a near-α titanium alloy Ti60 plate, Mater. Sci. Eng. A 688 (2017) 322–329, https://doi.org/10.1016/j.msea.2017.01.098.
[18] Z. Zhang, J. Fan, R. Li, H. Kou, Z. Chen, Q. Wang, H. Zhang, J. Wang, Q. Gao, J. Li, Orientation dependent behavior of tensile-creep deformation of hot rolled Ti65 titanium alloy sheet, J. Mater. Sci. Technol. 75 (2021) 265–275, https://doi.org/10.1016/j.jmst.2020.10.021.
[19] M. Higashi, T. Ozaki, Selective laser melting of pure molybdenum: Evolution of defect and crystallographic texture with process parameters, Mater. Des. 191 (2020) 108588, https://doi.org/10.1016/j.matdes.2020.108588.

[20] T.M. Rodgers, J.D. Madison, V. Tikare, Simulation of metal additive manufacturing microstructures using kinetic Monte Carlo, Comput. Mater. Sci. 135 (2017) 78–89, https://doi.org/10.1016/j.commatsci.2017.03.053.

[21] S. Saghafi, M.J. Withford, Z. Ghoranneviss, Characterizing flat-top laser beams using standard beam parameters, Can. J. Phys. 84 (2006) 223–240, https://doi.org/10.1139/p06-012.

[22] D.E. Jodi, T. Kitashima, M. Watanabe, Effect of scan strategy on the formation of a pure nickel single-crystal structure using a flat-top laser beam via laser powder bed fusion, Sci. Technol. Adv. Mater. 24 (2023) 2201380, https://doi.org/10.1080/14686996.2023.2201380.

[23] M. Rappaz, C.-A. Gandin, Probabilistic modelling of microstructure formation in solidification processes, Acta Metall. Mater. 41 (1993) 345–360, https://doi.org/10.1016/0956-7151(93)90065-Z.

[24] R.W. Messler, Principles of Welding, Wiley, New York, 2008.

[25] C. Körner, M. Markl, J.A. Koepf, Modeling and simulation of microstructure evolution for additive manufacturing of metals: a critical review, Metall. Mater. Trans. A 51 (2020) 4970–4983, https://doi.org/10.1007/s11661-020-05946-3.

[26] S.L. Lu, C.J. Todaro, Y.Y. Sun, T. Song, M. Brandt, M. Qian, Variant selection in additively manufactured alpha-beta titanium alloys, J. Mater. Sci. Technol. 113 (2022) 14–21, https://doi.org/10.1016/j.jmst.2021.10.021.

[27] C.M. Cepeda-Jiménez, F. Potenza, E. Magalini, V. Luchin, A. Molinari, M.T. Pérez-Prado, Effect of energy density on the microstructure and texture evolution of Ti-6Al-4V manufactured by laser powder bed fusion, Mater. Charact. 163 (2020) 110238, https://doi.org/10.1016/j.matchar.2020.110238.

[28] J. Liu, G. Li, Q. Sun, H. Li, J. Sun, X. Wang, Understanding the effect of scanning strategies on the microstructure and crystallographic texture of Ti–6Al–4V alloy manufactured by laser powder bed fusion, J. Mater. Process. Technol. 299 (2022) 117366, https://doi.org/10.1016/j.jmatprotec.2021.117366.

[29] S. Pilz, T. Gustmann, F. Günther, M. Zimmermann, U. Kühn, A. Gebert, Controlling the Young's modulus of a ß-type Ti-Nb alloy via strong texturing by LPBF, Mater. Des. 216 (2022) 110516, https://doi.org/10.1016/j.matdes.2022.110516.

[30] Y. Yang, Y.J. Liu, J. Chen, H.L. Wang, Z.Q. Zhang, Y.J. Lu, S.Q. Wu, J.X. Lin, Crystallographic features of α variants and β phase for Ti–6Al–4V alloy fabricated by selective laser melting, Mater. Sci. and Eng. A 707 (2017) 548–558, https://doi.org/10.1016/j.msea.2017.09.068.

[31] S.H. Sun, K. Hagihara, T. Nakano, Effect of scanning strategy on texture formation in Ni–25at.%Mo alloys fabricated by selective laser melting, Mater. Des. 140 (2018) 307–316, https://doi.org/10.1016/j.matdes.2017.11.060.

[32] S. Tekumalla, J.E. Chew, S.W. Tan, M. Krishnan, M. Seita, Towards 3-D texture control in a β titanium alloy via laser powder bed fusion and its implications on mechanical properties, Addit. Manuf. 59 (2022) 103111, https://doi.org/10.1016/j.addma.2022.103111.

[33] H. Lu, J. Pan, Y. Gu, J. Xiao, C. Ma, N. Yu, H. Li, Comparison of melt evolution and flow mechanisms of Inconel 718, Ti6Al4V, 304 stainless steel, and AlSi10Mg manufactured by laser powder bed fusion, structures, and properties after heat treatments, Mater. Sci. Eng. A 865 (2023) 144649, https://doi.org/10.1016/j.msea.2023.144649.

[34] J. Romano, L. Ladani, J. Razmi, M. Sadowski, Temperature distribution and melt geometry in laser and electron-beam melting processes – A comparison among common materials, Addit. Manuf. 8 (2015) 1–11, https://doi.org/10.1016/j.addma.2015.07.003.

[35] S.C. Wang, M. Aindow, M.J. Starink, Effect of self-accommodation on α/α boundary populations in pure titanium, Acta Mater. 51 (2003) 2485–2503, https://doi.org/10.1016/S1359-6454(03)00035-1.

[36] W.G. Burgers, On the process of transition of the cubic-body-centered modification into the hexagonal-close-packed modification of zirconium, Physica 1 (1934) 561–586, https://doi.org/10.1016/S0031-8914(34)80244-3.

[37] E. Lee, R. Banerjee, S. Kar, D. Bhattacharyya, H.L. Fraser, Selection of α variants during microstructural evolution in α/β titanium alloys, Philos. Mag. 87 (2007) 3615–3627, https://doi.org/10.1080/14786430701373672.

[38] S. Balachandran, A. Kashiwar, A. Choudhury, D. Banerjee, R. Shi, Y. Wang, On variant distribution and coarsening behavior of the α phase in a metastable β titanium alloy, Acta Mater. 106 (2016) 374–387, https://doi.org/10.1016/j.actamat.2016.01.023.

[39] D. Qiu, R. Shi, D. Zhang, W. Lu, Y. Wang, Variant selection by dislocations during α precipitation in α/β titanium alloys, Acta Mater. 88 (2015) 218–231, https://doi.org/10.1016/j.actamat.2014.12.044.

[40] D. Bhattacharyya, G.B. Viswanathan, R. Denkenberger, D. Furrer, H.L. Fraser, The role of crystallographic and geometrical relationships between α and β phases in an α/β titanium alloy, Acta Mater. 51 (2003) 4679–4691, https://doi.org/10.1016/S1359-6454(03)00179-4.

[41] D. Bhattacharyya, G.B. Viswanathan, H.L. Fraser, Crystallographic and morphological relationships between β phase and the Widmanstätten and allotriomorphic α phase at special β grain boundaries in an α/β titanium alloy, Acta Mater. 55 (2007) 6765–6778, https://doi.org/10.1016/j.actamat.2007.08.029.

[42] J. Liu, K. Zhang, Y. Yang, H. Wang, Y. Zhu, A. Huang, Grain boundary α-phase precipitation and coarsening: Comparing laser powder bed fusion with as-cast Ti-6Al-4V, Scripta Mater. 207 (2022) 114261, https://doi.org/10.1016/j.scriptamat.2021.114261.

[43] M. Salib, J. Teixeira, L. Germain, E. Lamielle, N. Gey, E. Aeby-Gautier, Influence of transformation temperature on microtexture formation associated with α precipitation at β grain boundaries in a β metastable titanium alloy, Acta Mater. 61 (2013) 3758–3768, https://doi.org/10.1016/j.actamat.2013.03.007.

[44] R. Shi, V. Dixit, G.B. Viswanathan, H.L. Fraser, Y. Wang, Experimental assessment of variant selection rules for grain boundary α in titanium alloys, Acta Mater. 102 (2016) 197–211, https://doi.org/10.1016/j.actamat.2015.09.021.

[45] N. Stanford, P.S. Bate, Crystallographic variant selection in Ti–6Al–4V, Acta Mater. 52 (2004) 5215–5224, https://doi.org/10.1016/j.actamat.2004.07.034.

[46] R. Banerjee, D. Bhattacharyya, P.C. Collins, G.B. Viswanathan, H.L. Fraser, Precipitation of grain boundary α in a laser deposited compositionally graded Ti–8Al–xV alloy – An orientation microscopy study, Acta Mater. 52 (2004) 377–385, https://doi.org/10.1016/j.actamat.2003.09.038.

[47] T. Furuhara, S. Takagi, H. Watanabe, T. Maki, Crystallography of grain boundary α precipitates in a β titanium alloy, Metall. Mater. Trans. A 27 (1996) 1635–1646, https://doi.org/10.1007/BF02649821.

[48] I. Lonardelli, N. Gey, H.-R. Wenk, M. Humbert, S.C. Vogel, L. Lutterotti, In situ observation of texture evolution during α→β and β→α phase transformations in titanium alloys investigated by neutron diffraction, Acta Mater. 55 (2007) 5718–5727, https://doi.org/10.1016/j.actamat.2007.06.017.

[49] G.C. Obasi, S. Birosca, J.Q. Quinta da Fonseca, M. Preuss, Effect of β grain growth on variant selection and texture memory effect during α→β→α phase transformation in Ti–6 Al–4 V, Acta Mater. 60 (2012) 1048–1058, https://doi.org/10.1016/j.actamat.2011.10.038.

[50] D. Banerjee, J.C. Williams, Perspectives on titanium science and technology, Acta Mater. 61 (2013) 844–879, https://doi.org/10.1016/j.actamat.2012.10.043.

[51] S.L. Semiatin, K.T. Kinsel, A.L. Pilchak, G.A. Sargent, Effect of process variables on transformation-texture development in Ti–6Al–4V sheet following beta heat treatment, Metall. Mater. Trans. A 44 (2013) 3852–3865, https://doi.org/10.1007/s11661-013-1735-6.

[52] S. Banerjee, P. Mukhopadhyay, Phase Transformations: Examples from Titanium and Zirconium Alloys, Elsevier, Amsterdam, 2007.

[53] L. Zeng, T.R. Bieler, Effects of working, heat treatment, and aging on microstructural evolution and crystallographic texture of α, α′, α″ and β phases in Ti–6Al–4V wire, Mater. Sci. Eng. A 392 (2005) 403–414, https://doi.org/10.1016/j.msea.2004.09.072.

[54] M. Sabeena, S. Murugesan, P. Anees, E. Mohandas, M. Vijayalakshmi, Crystal structure and bonding characteristics of transformation products of bcc β in Ti-Mo alloys, J. Alloys Compd. 705 (2017) 769–781, https://doi.org/10.1016/j.jallcom.2016.12.155.

[55] M. Young, E. Levine, H. Margolin, The aging behavior of orthorhombic martensite in Ti-6-2-4-6, Metall. Trans. 5 (1974) 1891–1898, https://doi.org/10.1007/BF02644157.

[56] L. Meng, T. Kitashima, T. Tsuchiyama, M. Watanabe, β-texture evolution of a near-β titanium alloy during cooling after forging in the β single-phase and (α + β) dual-phase regions, Metall. Mater. Trans. A 52 (2021) 303–315, https://doi.org/10.1007/s11661-020-06060-0.

[57] M.A. Chaudry, G. Mohr, K. Hilgenberg, Experimental and numerical comparison of heat accumulation during laser powder bed fusion of 316L stainless steel, Prog. Addit. Manuf. 7 (2022) 1071–1083, https://doi.org/10.1007/s40964-022-00282-x.

[58] S.A. Oh, R.E. Lim, J.W. Aroh, A.C. Chuang, B.J. Gould, B. Amin-Ahmadi, J. V. Bernier, T. Sun, P.C. Pistorius, R.M. Suter, A.D. Rollett, High speed synchrotron X-ray diffraction experiments resolve microstructure and phase transformation in laser processed Ti–6Al–4V, Mater. Res. Lett. 9 (2021) 429–436, https://doi.org/10.1080/21663831.2021.1966537.

[59] M. Chen, S. Van Petegem, Z. Zou, M. Simonelli, Y.Y. Tse, C.S.T. Chang, M. G. Makowska, D.F. Ferreira Sanchez, H. Moens-Van Swygenhoven, Microstructural engineering of a dual-phase Ti–Al–V–Fe alloy via in situ alloying during laser powder bed fusion, Addit. Manuf. 59 (2022) 103173, https://doi.org/10.1016/j.addma.2022.103173.

[60] S. Le Corre, R. Forestier, F. Brisset, M. Mathon, D. Solas, Influence of β-forging on texture Development in Ti 6246 alloy, in: Proc. 13th world conference, Titan, Wiley Online Library, 2016, pp. 759–764, https://doi.org/10.1002/9781119296126.ch127.

[61] Y. Wang, J. Shi, Developing very strong texture in a nickel-based superalloy by selective laser melting with an ultra-high power and flat-top laser beam, Mater. Charact. 165 (2020) 110372, https://doi.org/10.1016/j.matchar.2020.110372.

[62] T. Ishimoto, K. Hagihara, K. Hisamoto, S.H. Sun, T. Nakano, Crystallographic texture control of beta-type Ti–15Mo–5Zr–3Al alloy by selective laser melting for the development of novel implants with a biocompatible low Young's modulus, Scripta Mater. 132 (2017) 34–38, https://doi.org/10.1016/j.scriptamat.2016.12.038.

[63] L.R. Goossens, B. Van Hooreweder, A virtual sensing approach for monitoring melt-pool dimensions using high speed coaxial imaging during laser powder bed fusion of metals, Addit. Manuf. 40 (2021) 101923, https://doi.org/10.1016/j.addma.2021.101923.

[64] S. Ghosh, L. Ma, L.E. Levine, R.E. Ricker, M.R. Stoudt, J.C. Heigel, J.E. Guyer, Single-track melt-pool measurements and microstructures in Inconel 625, JOM 70 (2018) 1011–1016, https://doi.org/10.1007/s11837-018-2771-x.

[65] Y. Zhang, J. Zhang, Modeling of solidification microstructure evolution in laser powder bed fusion fabricated 316L stainless steel using combined computational fluid dynamics and cellular automata, Addit. Manuf. 28 (2019) 750–765, https://doi.org/10.1016/j.addma.2019.06.024.

[66] K. Wang, D. Xie, F. Lv, F. Liu, R. Liu, D. Liu, J. Zhao, Stability of molten pool and microstructure evolution of Ti-6Al-4 V during laser powder bed fusion with a flat-top beam, Addit. Manuf. 75 (2023) 103756, https://doi.org/10.1016/j.addma.2023.103756.

[67] W. Yuan, H. Chen, S. Li, Y. Heng, S. Yin, Q. Wei, Understanding of adopting flat-top laser in laser powder bed fusion processed Inconel 718 alloy: simulation of single-track scanning and experiment, J. Mater. Res. Technol. 16 (2022) 1388–1401, https://doi.org/10.1016/j.jmrt.2021.12.077.

[68] R. Li, J. Liu, Y. Shi, L. Wang, W. Jiang, Balling behavior of stainless steel and nickel powder during selective laser melting process, Int. J. Adv. Manuf. Technol. 59 (2012) 1025–1035, https://doi.org/10.1007/s00170-011-3566-1.

[69] S.H. Sun, K. Hagihara, T. Ishimoto, R. Suganuma, Y.F. Xue, T. Nakano, Comparison of microstructure, crystallographic texture, and mechanical properties in Ti–15Mo–5Zr–3Al alloys fabricated via electron and laser beam powder bed fusion technologies, Addit. Manuf. 47 (2021) 102329, https://doi.org/10.1016/j.addma.2021.102329.

[70] K. Nishimoto, K. Saida, Y. Fujita, Crystal growth in laser surface melting and cladding of Ni-base single crystal superalloy, Weld. World 52 (2008) 64–78, https://doi.org/10.1007/BF03266642.

[71] L. Wang, N. Wang, Effect of substrate orientation on the formation of equiaxed stray grains in laser surface remelted single crystal superalloys: Experimental investigation, Acta Mater. 104 (2016) 250–258, https://doi.org/10.1016/j.actamat.2015.11.018.

[72] N. Gey, M. Humbert, Characterization of the variant selection occurring during the α→β→α phase transformations of a cold rolled titanium sheet, Acta Mater. 50 (2002) 277–287, https://doi.org/10.1016/S1359-6454(01)00351-2.

[73] R. Demott, N. Haghdadi, X. Liao, S.P. Ringer, S. Primig, 3D characterization of microstructural evolution and variant selection in additively manufactured Ti-6Al-4 V, J. Mater. Sci. 56 (2021) 14763–14782, https://doi.org/10.1007/s10853-021-06216-2.

[74] M. Fu, Y. Yuan, X. Ma, X. Lin, A study of α variant selection in laser solid forming Ti–6Al–4V, J. Alloys Compd. 792 (2019) 1261–1266, https://doi.org/10.1016/j.jallcom.2019.04.052.

[75] T. Karthikeyan, A. Dasgupta, R. Khatirkar, S. Saroja, I. Samajdar, M. Vijayalakshmi, Effect of cooling rate on transformation texture and variant selection during β→α transformation in Ti–5Ta–1.8Nb alloy, Mater. Sci. Eng. A 528 (2010) 549–558, https://doi.org/10.1016/j.msea.2010.09.055.

[76] D.E. Jodi, T. Kitashima, A. Singh, M. Watanabe, High-temperature microstructural stability of pure Ni fabricated by laser powder bed fusion using Gaussian and flat-top beam profiles, Mater. Charact. 200 (2023) 112897, https://doi.org/10.1016/j.matchar.2023.112897.